Journal of Applied Electrochemistry
https://doi.org/10.1007/s10800-017-1136-4

RESEARCH ARTICLE

Combustion combined with ball milling to produce nanoscale La_2O_3 coated on $LiMn_2O_4$ for optimized Li-ion storage performance at high temperature

Yannan Zhang[1] · Peng Dong[1] · Mingyu Zhang[2] · Xueliang Sun[3] · Xiaohua Yu[4] · Jinjie Song[5] · Qi Meng[1] · Xue Li[1] · Yingjie Zhang[1]

Received: 29 August 2017 / Accepted: 4 December 2017

Abstract

In this study, La_2O_3 is synthesized by combustion method and then subjected to ultrafine ball milling to obtain La_2O_3 nanoparticles. In neopentyl glycol, La_2O_3 nanoparticles are coated on the surface of spinel $LiMn_2O_4$ ultimately obtaining La_2O_3 coating contents of 1.5, 3, 4.5, and 6 wt%. XRD characterization reveals that the nano La_2O_3 exhibits a favorable crystalline intensity, without impurities and the crystalline peak of La_2O_3 can be observed when the coating content is of up to 6 wt%. Successful deposition of a thin layer of La_2O_3 on the $LiMn_2O_4$ surface is confirmed by scanning electron microscopy, transmission electron microscopy, X-ray spectrum elemental plane scanning, and line scanning. Furthermore, inductively coupled plasma emission spectrography and electrochemical impedance spectroscopy analyses show that the nano-La_2O_3 coating significantly relieves the dissolution of Mn in $LiMn_2O_4$ materials, and also improves the electro-conductivity. The electrochemical performances of the coated $LiMn_2O_4$ samples are also investigated in this work. Compared with the pristine $LiMn_2O_4$, the $LiMn_2O_4$ coated with 3 wt% La_2O_3 exhibits a higher rate capability and better reversibility, exhibiting 103.5 and 90.6 mAh g^{-1} at 5 and 10 °C, respectively. After 100 cycles at 60 and 1 °C, the 3 wt% nano-La_2O_3-coated sample still exhibits a high-capacity retention of 91.68%.

Graphical Abstract

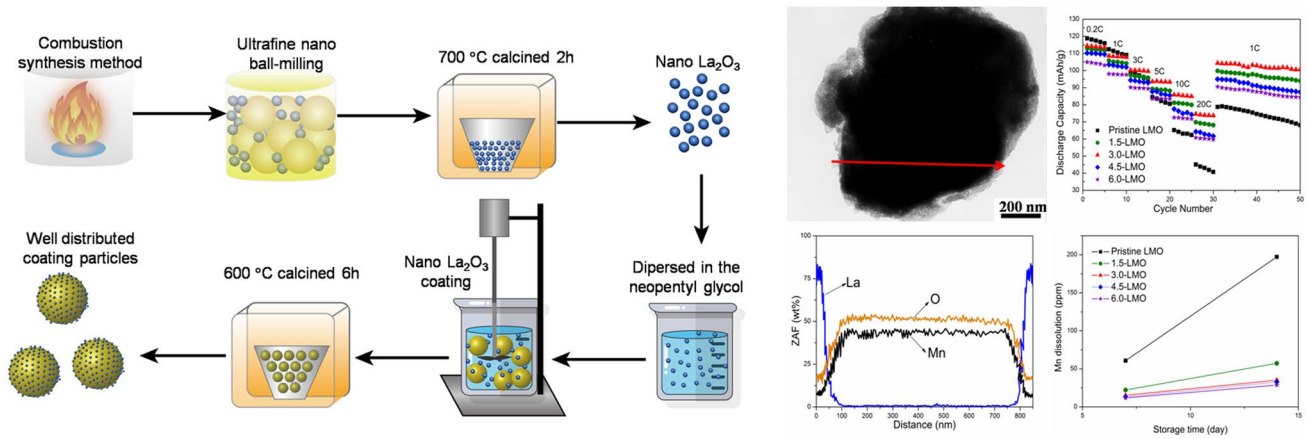

Keywords Combustion method · La_2O_3 coating · ICP-AES · Capacity retention

Extended author information available on the last page of the article

Published online: 12 December 2017

1 Introduction

Lithium-ion batteries are currently one of the most important renewable energy sources and are widely used in electric vehicles, hybrid vehicles, energy storage facilities, electronic appliances, and other applications [1–3]. Spinel lithium manganate has an important role in the development of lithium-ion battery materials owing to its low resource cost, high-voltage platform, stable electrochemical properties, high-safety, non-toxicity, and environmental friendliness [4–6]. However, certain defects limit its widespread applications in power batteries. On the one hand, Mn^{3+} undergoes Jahn–Teller distortion in the charge/discharge process, resulting in abrupt changes of the spinel structure into a tetragonal phase, which causes an abrupt volume change that produce microstress, thereby leading to decreased stability and capacity of the material [7, 8]. On the other hand, Mn^{3+} in $LiMn_2O_4$ undergoes a disproportionation reaction, and the resulting Mn^{2+} is dissolved in the organic electrolyte and can cause loss of active substances from the electrode [9, 10]. In addition, Mn^{4+} is easily oxidized, which induces oxidative decomposition of the electrolyte to form Li_2CO_3 and other by-products around the active substances, thereby resulting in the battery's increased internal impedance and intensified capacity attenuation. This phenomenon is especially severe at high temperatures [11, 12].

Surface coating can prevent the direct contact of spinel $LiMn_2O_4$ with the electrolyte, consume the byproduct HF from the reaction of the material with the electrolyte, and suppress electrode material erosion by HF, which is one of the most effective means of improving the high-temperature cycling stability of $LiMn_2O_4$ [13, 14]. Considerable research efforts have been devoted to the surface modification of $LiMn_2O_4$, such as using Al_2O_3 [15], ZnO [16], TiO_2 [17], ZrO_2 [18], MgO [19], phosphates [20], solid electrolyte polymers [21], carbon materials [22], fluorides [23, 24], and other lithium electrode materials [25]. Mohan et al. coated $LiMn_2O_4$ with $LaPO_4$ to increase the 100th cycle capacity retention of the material at 50 °C to 82% from 56% [26]. Zhao et al. improved the rate performance of $LiMn_2O_4$ by ZrO_2 atomic deposition surface modification and the 100th cycle capacity retention of at 5 °C rate thus was 71.1% [27]. Zhang et al. used solid electrolyte $LiNbO_3$ to coat $LiMn_2O_4$, which markedly reduced the charge transfer impedance of $LiMn_2O_4$ and improved its rate performance in aqueous electrolytes [28].

La_2O_3 has exhibited favorable resistances to both acid corrosion and oxidation at high temperatures, and as a rare earth oxide, it can be used as an excellent lithium ion-conducting medium as well [29, 30]. Coating modification of spinel $LiMn_2O_4$ with La_2O_3 offers much promise to advance the function of active cathode materials in organic electrolyte environments. Arumugam et al. reported the use of lanthanum nitrate as the raw material for a La_2O_3 coating modification of $LiMn_2O_4$, which improved the 100th cycle capacity retention of $LiMn_2O_4$ at 30 °C from 60 to 86.3% [31]. Similarly, Feng et al. also used $LaNO_3$ as the lanthanum source to coat $LiMn_2O_4$ with 5 wt% La_2O_3; as a result, they obtained an excellent cathode material, with a high-capacity retention of 82.6% after 100 cycles at 60 °C [32].

The previously reported La_2O_3 coatings were all carried out in nitrate solutions, which needed to be filtered several times and may still have contained impurities such as N in the coating process. In this work, we report an innovative approach of coating $LiMn_2O_4$ with nano-La_2O_3 that is prepared by combining combustion synthesis and ultrafine ball milling after neopentyl glycol dispersion, rather than using the conventional nitrate solution for rare earth oxide coating. Ultimately, a uniform, highly crystalline nano-La_2O_3 layer is formed on the surface of spinel $LiMn_2O_4$ to provide a protective coating against acid corrosion and oxidation at high temperatures. The proposed method significantly improves the cycle life and rate performance of $LiMn_2O_4$, so that the material can charge and discharge stably even at elevated temperatures and high rates (20 °C in this work).

2 Experimental methods

2.1 Preparation of nano-La_2O_3

Certain amounts of the raw materials lanthanum nitrate hexahydrate (Aldrich), glycerol (Aldrich), and polyethylene glycol (Aldrich) (molar ratio of 12:13:1) were dissolved in deionized water, and the pH was adjusted to 8.0 by dropwise addition of dilute nitric acid (0.1 mol/L) after thorough mixing with a high-speed magnetic stirrer. The mixed solution was then heated in the electric furnace. With the rising temperature, the solution finally converted into a white resinous gel. With continuous heating, the gel combusted spontaneously and jetted out with white powders. The resulting white powders were ground in an ultrafine ball mill (Fritsch Pulverisette7) for 2 h, followed by calcining at 700 °C for 2 h to produce nano-La_2O_3 powders.

2.2 Preparation of spinel $LiMn_2O_4$

The $LiMn_2O_4$ powders were synthesized by high-pressure spray drying assisted with solid-phase sintering. Li_2CO_3 (Tianqi) and electrolytic MnO_2 (Aldrich) were mixed in deionized water at a Li:Mn molar ratio of 1.05:2, after ball milling with a vertical ball mill for 2 h. The mixture was then subjected to high-pressure spray drying (compressed air

pressure of 18.5 MPa, inlet temperature of 280 °C, and outlet temperature of 105 °C), followed by calcination at 850 °C for 12 h to yield pristine $LiMn_2O_4$ powders.

2.3 Preparation of nano-La_2O_3-coated spinel $LiMn_2O_4$

The La_2O_3-coated $LiMn_2O_4$ material was prepared by coating 10 g of $LiMn_2O_4$ material with different mass percentages of La_2O_3 (1.5, 3, 4.5, and 6 wt%) in neopentyl glycol solution. The 1.5, 3, 4.5, and 6 wt% La_2O_3 were separately dissolved in 100 mL of neopentyl glycol solutions and thoroughly stirred to uniformly disperse the powders; the pH of each solution was adjusted to 8.0 with dilute aqueous ammonia. 10 g of $LiMn_2O_4$ was added slowly to each of the mixed solutions, and the mixtures were stirred continuously, heated to 70 °C, and held for 8 h, until the moisture was evaporated to desiccation. After washing with deionized water and filtering, the resulting xerogel was dried in an oven at 120 °C for 12 h. Finally, the dried product was heat treated at 600 °C for 8 h to yield $LiMn_2O_4$ cathode materials coated with different contents (1.5, 3, 4.5, and 6 wt%) of La_2O_3, which were labeled as 1.5-LMO, 3-LMO, 4.5-LMO, and 6-LMO, respectively. A schematic diagram of the coating process is shown in Fig. 1.

2.4 Physical characterization

The phase structures of samples were observed by X-ray diffractometer (Rigaku, Rint-2000, Cu-K-α radiation) in a scanning range 2θ of 10°–80° and a scanning rate of 2°/min. The surface morphologies of the samples were observed by scanning electron microscopy (SEM, TESCAN VEGA 3), while the microstructures were observed by transmission electron microscopy (TEM, JEOL JEM-2010). The contents of various elements in the coating layers and the amounts of Mn ion dissolved in the electrolytes were measured with an inductively coupled plasma emission spectrograph (ICP, Thermo-6000).

2.5 Electrochemical characterization

For the battery assembly test, the pristine and coated (with four different contents of La_2O_3) $LiMn_2O_4$ active materials (80 wt%), the acetylene black conductive agent (10 wt%), and the polyvinylidene fluoride (PVDF, Aldrich) adhesive (10 wt%) were homogeneously mixed in a certain amount of *N*-methyl-2-pyrrolidone (NMP, Aldrich). The resulting slurries were coated on an aluminum foil and then vacuum dried at 100 °C for 12 h to obtain the battery cathode plates. All the cathode materials were cut into discs 14 mm in diameter with an active mass loading of about 2.2 mg cm^{-2}. Using metallic lithium as the anode, 1 M L^{-1} $LiPF_6$ was dissolved in ethylene carbonate (EC), dimethyl carbonate (DMC), and diethyl carbonate (DEC) with a volume ratio of 1:1:1 to serve as the electrolytes, which were assembled into 2025 cells in an argon-filled glove box with porous polyethylene film (Celgard 2400) as the separator. The cyclic charge/discharge test was conducted at 60 °C in a voltage range of 3.0–4.5 V using a LAND-CT2001A battery test

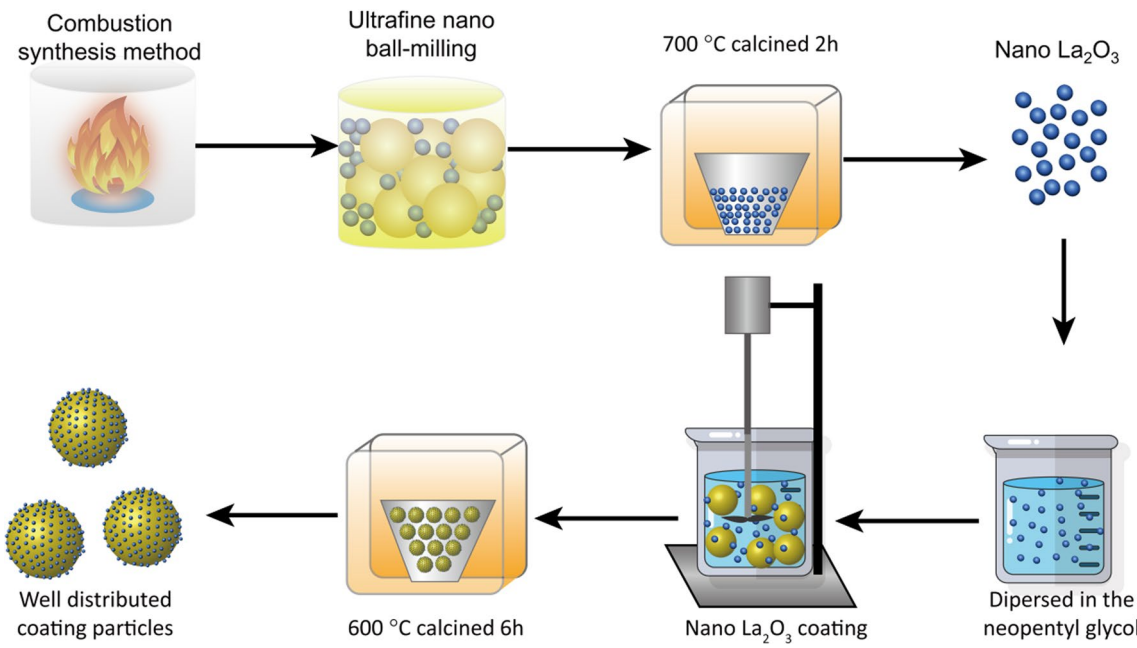

Fig. 1 Schematic diagram for the combustion preparation of nano La_2O_3-coated $LiMn_2O_4$

system. Electrochemical impedance spectroscopy (EIS) was performed using a PRISTON-P4000 workstation within a frequency range of 10 mHz–100 kHz and an AC amplitude of 5 mV.

3 Results and discussion

Figure 2a illustrates the XRD patterns of the nano-La_2O_3 prepared by the combustion method. As can be seen from the figure, the diffraction peaks of the samples correspond to the hexagonal lanthanum oxide standard card (JCPDS73-2141) [33]. No impurity peaks appear, indicating that the lanthanum nitrate has completely decomposed and synthesized pure La_2O_3 by glycerol-assisted combustion [34, 35]. Figure 2b illustrates the XRD patterns of all uncoated and La_2O_3-coated (1.5, 3, 4.5, and 6 wt%) samples. As can be seen from the figure, all the samples exhibit clear diffraction peaks before and after coating, each of which is identical with the standard card (JCPDS: 35-0782), belonging to the *Fd−3m* space group [36, 37]. This result suggests that the La_2O_3 coating layer does not affect the spinel structure of $LiMn_2O_4$ [38]. When the coating content is lower than 4.5 wt%, no heterogeneous phase and no La_2O_3 diffraction peak signal are detected because of the small amounts of coating. When the La_2O_3 content rises to 6 wt%, the characteristic La_2O_3 peaks are detected at positions of 26.16°, 29.16°, 39.57°, and 46.16°, indicating that $LiMn_2O_4$ particles are surface-coated with La_2O_3, which can be obtained by neopentyl glycol mixing and annealing at 600 °C.

Figure 3 displays the SEM images of La_2O_3 nanoparticles prepared by sintering before and after ultrafine ball milling. From Fig. 3a, the La_2O_3 particles prepared by the combustion method cluster together as non-uniform particles with sizes of 0.1–1 μm. After ultrafine ball milling and calcination at 700 °C, the La_2O_3 particles exhibit markedly reduced size, within approximately 10–20 nm, as well as smooth

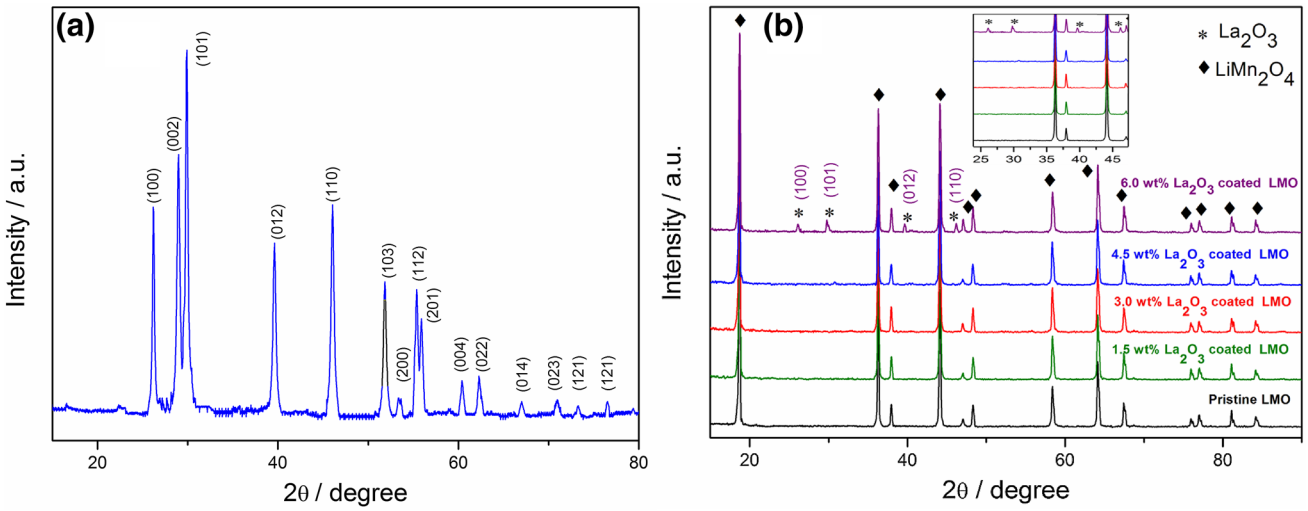

Fig. 2 **a** XRD patterns of the La_2O_3 powder samples prepared by combustion combined with ultrafine ball milling after sintering at 700 °C; **b** XRD patterns of the uncoated and La_2O_3-coated $LiMn_2O_4$ powder samples

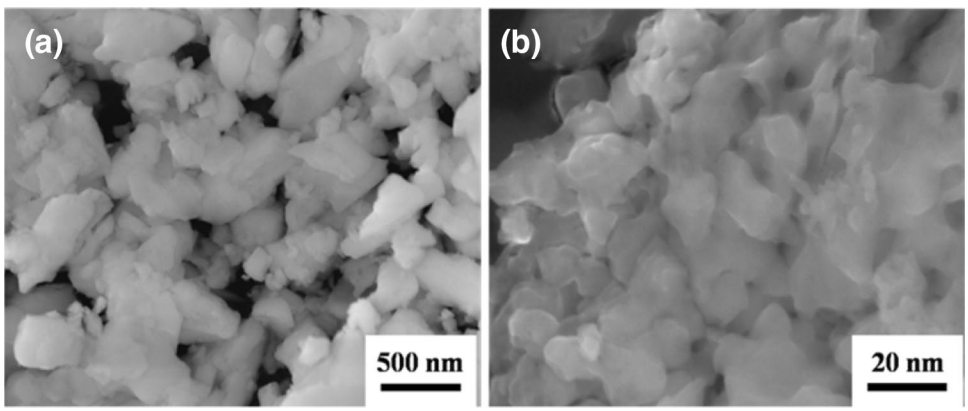

Fig. 3 SEM images: **a** La_2O_3 prepared by combustion synthesis without ball milling; **b** La_2O_3 obtained by sintering after nano-ball milling

surfaces, which facilitate their uniform dispersion and dissolution in the polyol solution, as shown in Fig. 3b.

Figure 4a shows the SEM image of uncoated $LiMn_2O_4$ material that is in the solid state synthesized by high-pressure spray drying. The $LiMn_2O_4$ primary particles synthesized by high-pressure spray drying clearly exhibit a polyhedral structure with particle size of 0.5–2 µm. In addition, secondary particles agglomerate into a spherical form. Figure 4b–e shows the SEM images of $LiMn_2O_4$ coated with 1.5, 3, 4.5, and 6 wt% La_2O_3, respectively. There is no obvious change in the morphology or size of the coated $LiMn_2O_4$ particles. With the increased coating amount, the coating layers on the $LiMn_2O_4$ particle surfaces become increasingly compact. As shown in Fig. 4e, the excessively high La_2O_3 content results in localized agglomeration of the La_2O_3 particles. Because the 3 wt% La_2O_3-coated sample presents the best electrochemical properties, this sample is subjected to a more detailed analysis in subsequent tests. Figure 4f presents the EDS pattern of the 3 wt% La_2O_3-coated sample, where the scanning area is within all the particle surface as shown in Fig. 4c. According to the EDS detection, the characteristic peaks of the major elements O, Mn, and La in the 3-LMO sample represent 38.8, 56.3, and 4.9% of the weight contents, respectively. Among these, the contents of Mn and O are significantly higher than La, which is attributed to the significantly higher depth of the SEM-EDS X-ray excitation (approximately 100–1000 nm) compared to the thickness of the La_2O_3 coating. It is clear from the figure that La is uniformly distributed on the surfaces of the $LiMn_2O_4$ particles [39].

To further investigate the coating layer of the most favorable sample, we perform TEM detection and local element line scanning on the $LiMn_2O_4$ samples before and after coating with 3 wt% La_2O_3, as shown in Fig. 5. The uncoated $LiMn_2O_4$ sample (Fig. 5a) exhibits a clear surface profile, whereas the coated sample (Fig. 5b) distinctly shows a uniform coating layer on its surface. As shown in Fig. 5c (a partial enlarged view of the coated sample), the coated particles on the surface are approximately 20–30 nm, and the La_2O_3 on the $LiMn_2O_4$ surface can be confirmed by selecting electron diffraction spots. The diffraction lattices (110) and (100) match well with the La_2O_3 phase (JCPDS73-2141), and therefore the nanoparticles on the coated $LiMn_2O_4$ surface can be confirmed to be La_2O_3 [40]. This coincides well with the analysis results of the previous SEM-EDS (Fig. 4). Moreover, the element line scanning is conducted on the coated sample following the direction of the horizontal arrow as shown in Fig. 5b. The line scanning results are shown in Fig. 5d. From the figure, the distributions of Mn, O, and La are clearly visible: La content is very high (75%) and is distributed evenly on both sides of the $LiMn_2O_4$ particle, whereas Mn content is below 20% on the left and right

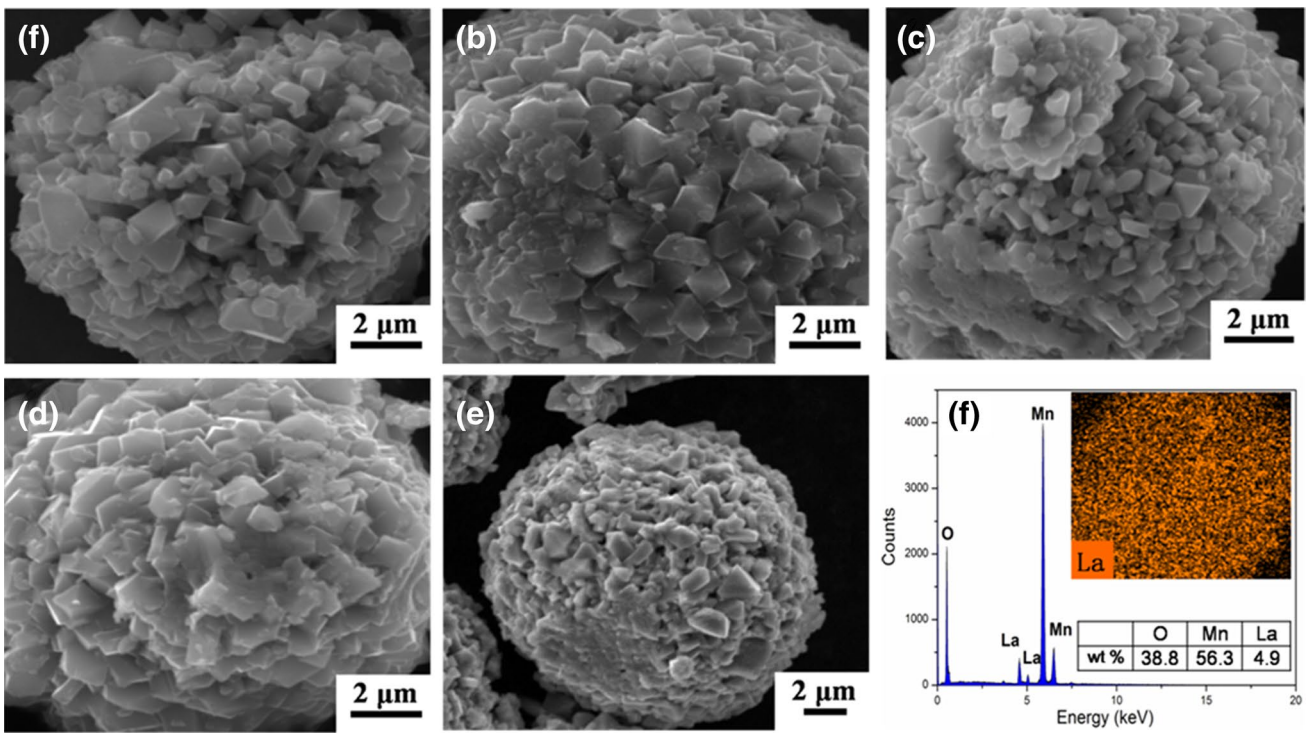

Fig. 4 SEM images: **a** Uncoated $LiMn_2O_4$; **b–e** $LiMn_2O$ coated with different La_2O_3 contents (1.5, 3, 4.5, and 6 wt%); **f** EDS pattern of the 3 wt% La_2O_3-coated $LiMn_2O_4$ sample

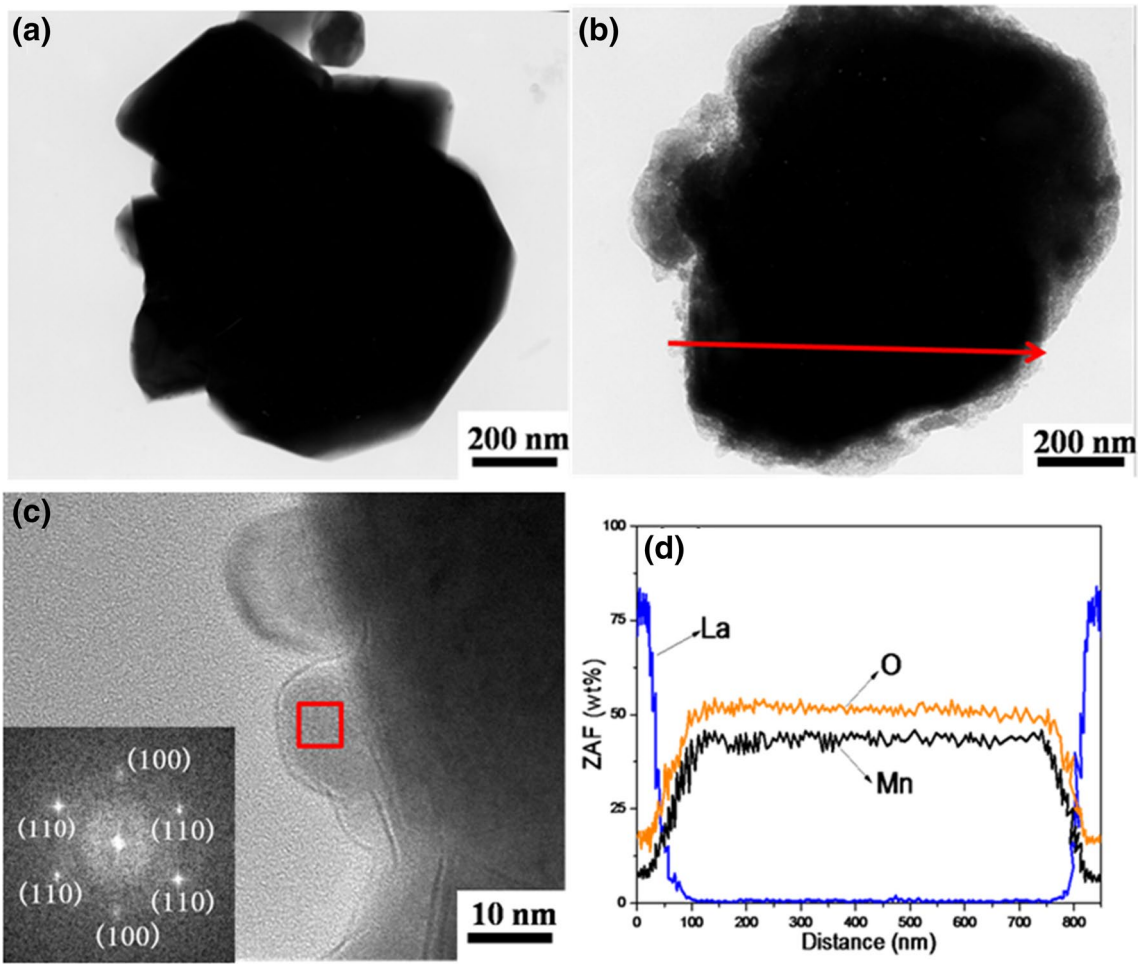

Fig. 5 TEM images: **a** Uncoated $LiMn_2O_4$; **b** 3 wt% La_2O_3-coated $LiMn_2O_4$; **c** Surface particles and SEAD pattern of 3 wt% La_2O_3-coated $LiMn_2O_4$; **d** Line scan image following the arrow in **b** from left to right

sides of the sample edge, indicating that a higher content of La_2O_3 coating layers forms homogeneously on the $LiMn_2O_4$ surface. The situation is completely opposite inside the sample, and the change in the O content is basically consistent with that of the Mn content. As La_2O_3 has advantages in thermal stability and favorable lithium ion conductivity, it is naturally expected that the surface modification with La_2O_3 will improve the electrochemical characteristics of $Li/LiMn_2O_4$ cells.

Figure 6 shows the XPS spectra of the Mn 2p and La 2d special regions for the pristine LMO and 3 wt% La_2O_3-coated samples. For the uncoated $LiMn_2O_4$ (Fig. 6a), the Mn $2p_{3/2}$ XPS binding energy for Mn^{4+} and Mn^{3+} is located at 641.6 and 642.7 eV, respectively. Meanwhile, the relative peak area associated with Mn^{4+} is increased after La_2O_3 coating (Fig. 6b), and as a result the 3-LMO electrode may show an increased Mn oxidation state relative to the pristine $LiMn_2O_4$ surface. According to the research of Hunter et al. [41, 42], an increased oxidation state of Mn should effectively alleviate the disproportionation reaction of Mn^{3+}, thereby improving the cycling performance of spinel $LiMn_2O_4$. Moreover, as shown in Fig. 6c, La $3d_{5/2}$ and La $3d_{5/2}$ peaks are located at 834.90 and 851.66 eV, respectively, with 16.76 eV of doublet separation for each peak, which can be assigned to the existence of La^{3+}. The high concentration of La^{3+} is also a strong evidence for the presence of La_2O_3 coatings.

The capacity/cycle number graphs of different $LiMn_2O_4$ samples at 60 °C are shown in Fig. 6a. In terms of the initial capacity ,the pristine $LiMn_2O_4$ shows higher values than the other La_2O_3-coated samples, because La_2O_3 is electrochemically inactive at 3.0–4.5 V versus Li^+/Li. As noted above, La_2O_3 particles grow gradually with increasing coating amounts. The mass of active material per unit area on the electrode is also reduced, leading to decreasing of the initial capacity. The specific capacity of uncoated pristine LMO decays to 61.76 mAh g^{-1} from the initial 113.23 mAh g^{-1} after 100 cycles (3.0–4.5 V and 1 °C) at 60 °C, showing

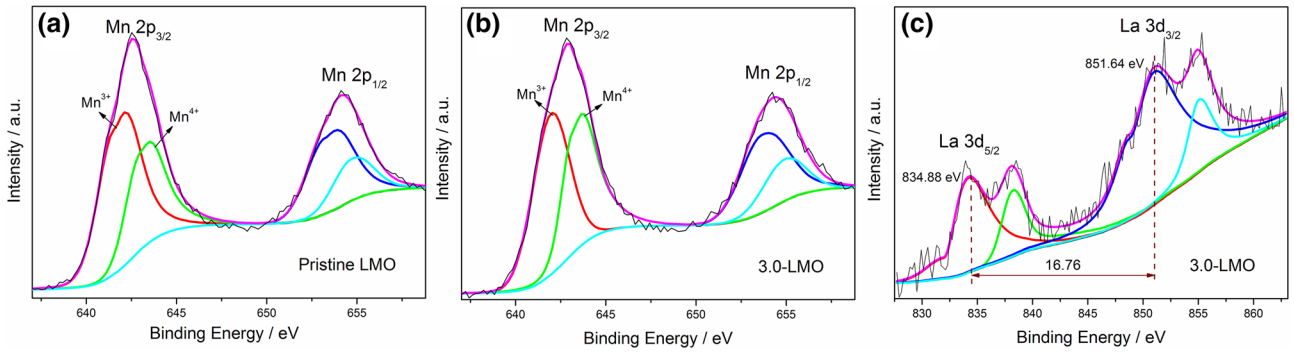

Fig. 6 XPS spectra of the Mn 2P special regions for **a** uncoated $LiMn_2O_4$; **b** 3 wt% La_2O_3-coated $LiMn_2O_4$; **c** XPS spectra of the La 2d special region for 3 wt% La_2O_3-coated $LiMn_2O_4$

a capacity retention of only 54.1%. Although samples 1.5-LMO, 3-LMO, 4.5-LMO, and 6-LMO have initial capacities lower than the pristine LMO after nano-La_2O_3 coating, their capacity retentions increase to 83.5, 91.7, 81.7, and 81.1%, respectively, which are significant improvements over the uncoated sample. The initial specific capacity of the 3 wt%-coated sample is 107.12 mAh g^{-1}, which remains 98.21 mAh g^{-1} after 100 cycles.

Furthermore, the electrochemical performance of the 3 wt% La_2O_3-coated sample is compared with that of other recently related reports in the literature (Table 1). Compared with these reports, our data apparently demonstrate that the capacity retention ability of $LiMn_2O_4$ is improved by the nano- La_2O_3 coating method.

To further evaluate the rate performance, different $LiMn_2O_4$ samples were subjected to charge/discharge cycle testing at 60 °C with different current densities. After 30 cycles from 0.2 to 20 °C, the rate returned to 1 °C. A rate of n C corresponds to a full charge/discharge rate of the theoretical capacity in 1/n hours, and 1 °C is 148 mAh g^{-1} for $LiMn_2O_4$. As shown in Fig. 7b, compared with the uncoated pristine $LiMn_2O_4$, the nano-La_2O_3-coated samples display better rate performance. With the increasing rate, the specific discharge capacities of 3-LMO reach 93.53 and 85.85 mAh g^{-1} at 5 and 10 °C, respectively. Even at 20 °C, the specific discharge capacity of 3-LMO remains up to 75.62 mAh g^{-1}, which is 66.16% of its initial 0.2 °C specific discharge capacity (114.30 mAh g^{-1}). In contrast, the uncoated sample has a specific discharge capacity of 45.11 mAh g^{-1} at 20 °C, accounting for only 37.97% of its initial 0.2 °C specific discharge capacity of 118.80 mAh g^{-1}. When the rate returns to 1 °C after discharging at a high rate (20 °C), the specific discharge capacities of samples 1.5-LMO, 3-LMO, 4.5-LMO, and 6-LMO are 99.85, 104.38, 95.01 and 90.58 mAh g^{-1}, respectively. Moreover, the samples can retain 91.70, 97.44, 96.74, and 91.39% of their initial 1 °C specific discharge capacities, respectively. Comparatively, the uncoated sample exhibits a specific discharge capacity of 78.75 mAh g^{-1}, retaining only up to 70.03% of the initial specific capacity. These results clearly demonstrate the amelioration of the capacity loss in the cycle after surface modification, indicating that the nano-La_2O_3 coating can facilitate the formation of a more compact ion conductive membrane, which can significantly improve the rate performance and cycling life of spinel $LiMn_2O_4$ [46, 47].

The fading of the $LiMn_2O_4$ material's capacity is mainly due to the following two factors: First, the electrolyte decomposes on the spinel material surface in the charge/discharge process to cause capacity fading [48]; second, according to Aurbach et al.'s latest research, Mn^{3+} is the dominant dissolved manganese cation in $LiPF_6$-based electrolyte solutions, and the resulting Mn

Table 1 Recently reported LIBs systems based on different materials modification of $LiMn_2O_4$

Coating materials of $LiMn_2O_4$	Capacity retention and discharge capacity (mAh g^{-1}) after several cycles at certain rate and temperature
2 wt% AlF_3 [23]	89.8%, 92.9, 100 cycles, 1, 25 °C
3 wt% TiO_2 [17]	62.0%, 77.1, 250 cycles, 1, 60 °C
3 wt% $Co_3(PO_4)_2$ [43]	87.0%, 112.8, 100 cycles, 1, 60 °C
2 wt% Lithium polyacrylate [44]	84.5%, 99.6, 50 cycles, 0.2, 55 °C
3 wt% AlP [45]	86.9%, 107.5, 100 cycles, 1, 60 °C
3 wt% La_2O_3(this work)	91.7%, 98.2, 100 cycles, 1, 60 °C

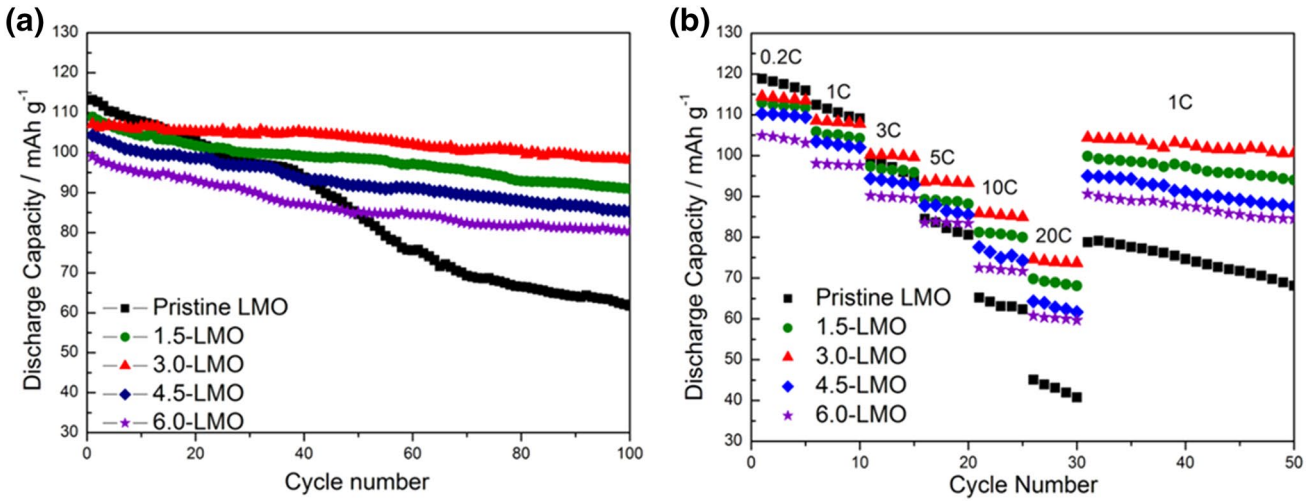

Fig. 7 **a** Charge/discharge cycle performance of the uncoated and La_2O_3-coated $LiMn_2O_4$ at 60 and 1 °C rate; **b** Rate performance of the uncoated and La_2O_3-coated $LiMn_2O_4$ at 60 °C

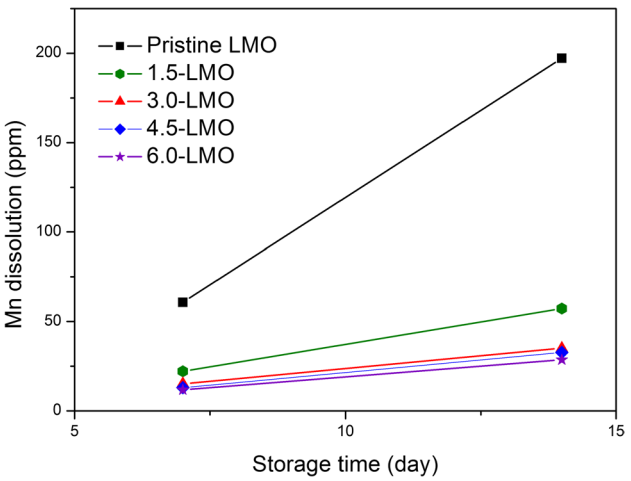

Fig. 8 Storage time in relation to the manganese ion dissolution in electrolyte for different samples stored at 60 °C

ions dissolved in the organic electrolyte cause loss of the active material from the electrode [49–51], thereby resulting in capacity fading. From the above analysis, the cycle and rate performances of materials are greatly improved after coating with nano-La_2O_3. The nano-particle coating layer can effectively prevent the electrolyte dissolution of Mn in spinel $LiMn_2O_4$, which is attributed to the favorable acid corrosion resistance and the stability of highly crystalline La_2O_3. To further verify this inference, the various uncoated and coated samples stored in electrolyte at 60 °C were subjected to ICP testing for Mn dissolution. As shown in Fig. 8, in all the samples at 60 °C, the electrolyte dissolution of Mn intensifies over time. After storage for 7 and 14 days, the pristine LMO exhibits the highest Mn concentrations in the electrolyte up to 60.8 and 197.2 ppm, respectively. Meanwhile, the Mn concentrations of samples 1.5-LMO, 3-LMO, 4.5-LMO, and 6-LMO are 22.2–57.3; 15.2–35.7; 13.1–32.7; and 11.8–28.6 ppm, respectively. This suggests that the nano-La_2O_3 coating can significantly reduce the manganese dissolution in electrolytes at high temperatures and suppress the generation of side reactions on the spinel $LiMn_2O_4$ surface, thereby improving the cycle and rate performances. The La_2O_3 contents in various samples were also detected by ICP test. The comparison of actual versus theoretical contents of La_2O_3 in Table 2 demonstrates that the errors in the coating amounts for the various samples are all within 10%,

Table 2 La_2O_3 contents of the prepared samples based on ICP results and the amounts of Mn dissolved in electrolytes of various samples after storage at 60 °C for 15 days

Sample name	La_2O_3 content (%)	Error from theoretical La_2O_3 content (%)	Amount of Mn dissolved in electrolyte (after storage for 14 days)
Pristine LMO	–	–	197.2
1.5-LMO	1.41	5.85	57.3
3.0-LMO	2.81	6.13	35.7
4.5-LMO	4.19	6.96	32.7
6.0-LMO	5.53	7.86	28.6

and the actual coating contents are all in accord with the theoretical prediction.

Figure 9 presents the Nyquist plots of the pristine LMO and 3-LMO samples after the 1st and 100th cycles at a 1 °C current density. Table 3 lists the results of various components after fitting the collected data using the equivalent circuit shown in Fig. 9c. The EIS of the pristine LMO and 3-LMO are composed of the cell contact resistance (Re) of the electrode and electrolyte, the resistance (Rsf) generated by the solid electrolyte membrane, the charge transfer resistance (Rct) at the electrode/electrolyte interface, and the Warburg impedance (W_1) [52]. As shown in Fig. 9a, b, the Re of the pristine LMO and 3-LMO both increase slightly after 100 cycles at high temperatures, mainly because poorly conductive substances (such as Li_2CO_3 and LiF) from side reactions are deposited on the electrode surface. However, the Re of 3-LMO is 7.9 Ω, which is lower than the 13.5 Ω of the pristine LMO, indicating that the nano-La_2O_3 coating can inhibit the occurrence of these side reactions. The Rsf of 3-LMO before and after cycling are all less than those of pristine LMO, suggesting that the La_2O_3 coating layer can prevent the thickness increase of the solid electrolyte interface membrane. The Rct increases more rapidly than the Rsf for 3-LMO. Moreover, the Rct of the pristine LMO increases to 1583.3 Ω, which is much larger than that of the La_2O_3-coated sample (376.1 Ω) after 100 cycles, which indicates that the nano-La_2O_3 coating can effectively improve the transfer rates of lithium ions and electrons at the electrode/electrolyte interface [53]. The coated material has a smaller Rct, which also can restrain undesirable side reactions between the electrode and electrolyte during the charge/discharge processes. These factors correspond to the favorable electrochemical cycle life and rate performance of the coated sample.

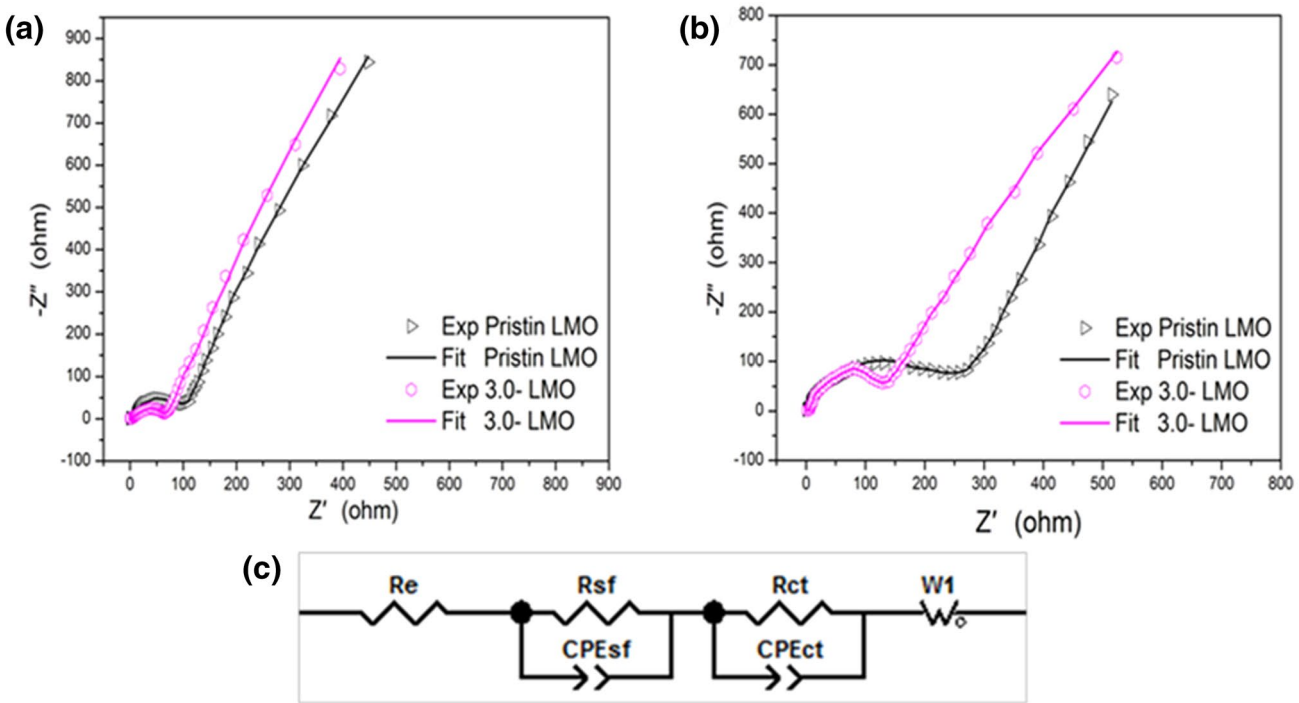

Fig. 9 EIS spectra of the pristine $LiMn_2O_4$ and 3-LMO tested **a** after 1st and **b** 100th charge/discharge cycles at the voltage of 3.0V. **c** Equivalent electrical circuit used for fitting the collected EIS data

Table 3 Fitted R_e, R_{sf}, and R_{ct} of pristine LMO and 3-LMO from EIS spectra using the equivalent circuit as shown in Fig. 9c

Cycle number	Pristine LMO				3-LMO			
	R_e (Ω)	R_{sf} (Ω)	R_{ct} (Ω)	CPE_{ct}	R_e (Ω)	R_{sf} (Ω)	R_{ct} (Ω)	CPE_{ct}
1st	6.2	78.5	185.8	1.682×10^{-5}	3.8	43.1	116.6	7.583×10^{-6}
100th	13.5	233.6	1583.3	8.689×10^{-5}	7.9	132.9	376.1	2.165×10^{-5}

4 Conclusion

In this work, pure La_2O_3 nanoparticles were directly synthesized by glycerol-assisted combustion combined with ultrafine ball milling. After dispersion in neopentyl glycol, the La_2O_3 nanoparticles were successfully coated on the surface of spinel $LiMn_2O_4$. The materials coated with different contents of nano-La_2O_3 exhibited a greater cycling stability than the uncoated ones: After 100 cycles at 60 °C and a rate of 1 °C, the capacity retention could be up to 91.68%, and at 20 °C rate, the discharge capacity still maintained at 76.1 mAh g^{-1}. Furthermore, we used SEM plane scanning, TEM line scanning, and ICP analysis to study the Mn dissolution in the electrolyte, and AC impedance testing to investigate the improvement contributed by the nano-La_2O_3 coating layer. The proposed method of preparing of nano-La_2O_3 and modifying the $LiMn_2O_4$ surface forms a uniform and highly crystalline La_2O_3 layer with a thickness of 20–30 nm on the surface of spinel material, as a result, the dissolution of Mn in the electrolyte is significantly suppressed at high temperatures. Meanwhile, the impedance of the material can be effectively reduced by the La_2O_3 coating, which also contributes to the improved electrochemical cycling and rate performances of $LiMn_2O_4$. Thus, we believe that the successful combination of combustion and ultrafine ball milling can produce La_2O_3 coatings on $LiMn_2O_4$ surfaces that may potentially enhance the electrochemical performances of other positive materials.

Acknowledgements Financial support from National Natural Science Foundation of China (Nos. 51604132, 51601081, and 51764029) and Provincial Natural Science Foundation of Yunnan (No.2017FB085) are gratefully acknowledged.

References

1. Dunn B, Kamath H, Tarascon JM (2011) Science 334:928–935
2. Goodenough JB, Park KS (2013) J Am Chem Soc 135:1167–1176
3. Xu WM, Yuan AB, Tian L, Wang YQ (2011) J Appl Electrochem 41:453–460
4. Zhang K, Han XP, Hu Z, Zhang XL, Tao ZL, Chen J (2015) Chem Soc Rev 44:699–728
5. Park OK, Cho Y, Lee S, Yoo HC, Song HK, Cho J (2011) Energy Environ Sci 4:1621–1633
6. Cupid DM, Lehmann T, Bergfeldt T, Berndt H, Seifert HJ (2013) J Mater Sci 48:3395–3403
7. Zhao M, Song X, Wang F, Dai W, Lu X (2011) Electrochim Acta 56:5673–5678
8. Lee MJ, Lee S, Oh P, Kim Y, Cho J (2014) Nano Lett 14:993–999
9. Jiang CH, Tang ZL, Wang ST, Zhang ZT (2017) J Power Sources 357:144–148
10. Peng K, Peng TF (2014) Ceram Int 40:15345–15349
11. Stiaszny B, Ziegler JC, Kraub EE, Schmidt JP, Ivers-Tiffée E (2014) J Power Sources 251:439–450
12. Tang W, Hou Y, Wang F, Liu L, Wu Y, Zhu K (2013) Nano Lett 13:2036–2040
13. Lee KT, Jeong S, Cho J (2013) Acc Chem Res 46:1161–1170
14. Wu F, Yushin G (2017) Energy Environ Sci 10:435–459
15. Waller GH, Brooke PD, Rainwater BH, Lai SY, Hu R, Ding Y, Alamgir FM, Sandhage KH, Liu ML (2016) J Power Sources 306:162–170
16. Liu DQ, Liu XQ, He ZZ (2007) J Alloys Compd 43:6387–6391
17. Zhang CC, Liu XY, Su QL, Wu JH, Huang T, Yu AS (2017) ACS Sustain Chem Eng 5:640–647
18. Hu SK, Cheng GH, Cheng MY, Hwang BJ, Santhanam R (2009) J Power Sources 188:564–569
19. Jin NC, Ying JR, Jiang CY, Wan CR (2013) J Funct Mater 28:133–138
20. Qing CB, Bai Y, Yang JM, Zhang WF (2011) Electrochimi Acta 56:6612–6618
21. Li JL, Zhu YQ, Wang L, Cao CB (2014) ACS Appl Mater Interfaces 6:18742–18750
22. Noh HK, Park HS, Jeong HY, Lee SU, Song HK (2014) Angew Chemie Int Ed 53:5059–5063
23. Tron A, Park YD, Mun J (2016) J Power Sources 325:360–364
24. Zhao S, Bai Y, Chang Q, Yang Y, Zhang W (2013) Electrochim Acta 108:727–735
25. Wang HE, Qian D, Lu ZG, Li YK (2012) J Alloys Compd 517:186–191
26. Mohan P, Kalaignan GP (2014) Ceram Int 40:1415–1421
27. Zhao J, Wang Y (2013) Nano Energy 2:882–889
28. Zhang ZJ, Chou SL, Gu QF, Liu HK, Li HJ, Ozawa K, Wang JZ (2014) ACS Appl Mater Interfaces 6:22155–22165
29. Zhao SZ, Zhou H, Zhou T, Zhang ZH, Lin PY, Ren LQ (2013) Corros Sci 67:75–81
30. Fan HQ, Li SY, Zhao ZC, Wang H, Shi ZC (2011) Corros Sci 53:3821–3831
31. Arumugam D, Kalaignan GP (2010) Mater Res Bull 45:1825–1831
32. Feng L, Wang S, Han L, Qin X, Wei H, Yang Y (2012) Mater Lett 78:116–119
33. Nowicki W, Piskuła ZS, Kuźma P, Kirszensztejn P (2017) J Sol-Gel Sci Technol 82:574–580
34. Niasaria MS, Hosseinzadeh G, Davar F (2011) J Alloys Compd 509:4098–4103
35. Hu C, Liu H, Dong W, Zhang Y, Bao G, Lao C, Wang ZL (2007) Adv Mater 19:470–474
36. Shaju KM, Bruce PG (2008) Chem Mater 20:5557–5562
37. Guo CX, Wang M, Chen T, Lou XW, Li CM (2011) Adv Energy Mater 1:736–741
38. Kim JS, Kim K, Cho W, Shin WH, Kanno R, Choi JW (2012) Nano Lett 12:6358–6365
39. Zhou Q, Zhang H, Chang F, Li H, Pan H, Xue W, Hu DY, Yang S (2015) J Ind Eng Chem 31:385–392
40. Huang P, Zhao YH, Zhang J, Zhu Y, Sun YH (2013) Nanoscale 5:10844–10848
41. Hunter JC (1981) J Solid State Chem 39:142–147
42. Jang DH, Oh SM (1997) J Electrochem Soc 144:3342–3348
43. Feng XY, Zhang JX, Yin LW (2016) Powder Technol 287:77–81
44. Zhang QT, Xie XL, Fan WF, Wang XM (2016) Ionics 22:2273–2280
45. Feng XY, Zhang JX, Yin LW (2016) Mater Res Bull 74:421–424
46. Hao X, Lin X, Lu W, Bartlett BM (2014) ACS Appl Mater Interfaces 6:10849–10857
47. Cho MY, Roh KC, Park SM, Lee JW (2011) Mater Lett 65:2011–2014
48. Lee S, Jeong M, Cho J (2013) Adv Energy Mater 3:1623–1629
49. Shi Y, Chou SL, Wang JZ, Wexler D. Li HJ, Liu HK, Wu Y (2012) J Mater Chem 22:16465–16470

50. Banerjee A, Shilina Y, Ziv B, Ziegelbauer JM, Luski S, Aurbach D, Halalay IC (2017) J Am Chem Soc 139:1738–1741
51. Shilina Y, Ziv B, Meir A, Banerjee A, Ruthstein S, Luski S, Aurbach D, Halalay IC (2017) Anal Chem 88:4440–4447
52. Peng ZD, Jiang QL, Du K, Wang WG, Hu GR, Liu YX (2010) J Alloys Compd 493:640–644
53. Lee S, Cho Y, Song HK, Lee KT, Cho J (2012) Angew Chemie Int Ed 51:8748–8752

Affiliations

Yannan Zhang[1] · Peng Dong[1] · Mingyu Zhang[2] · Xueliang Sun[3] · Xiaohua Yu[4] · Jinjie Song[5] · Qi Meng[1] · Xue Li[1] · Yingjie Zhang[1]

✉ Xue Li
438616074@qq.com

✉ Yingjie Zhang
zyjkmust@126.com

[1] National and Local Joint Engineering Laboratory for Lithium-ion Batteries and Materials Preparation Technology, Key Laboratory of Advanced Battery Materials of Yunnan Province, Kunming University of Science and Technology, Kunming 650093, China

[2] Yunnan Provincial Energy Research Institute Co., LTD., Kunming 650093, China

[3] Nanomaterials and Energy Lab, Department of Mechanical and Materials Engineering, University of Western Ontario, London, ON N6A 5B9, Canada

[4] National Engineering Research Center of Waste Resource Recovery, Kunming University of Science and Technology, Kunming 650093, China

[5] Key Laboratory of Mesoscale Severe Weather/Ministry of Education, and School of Atmospheric Sciences, Nanjing University, Nanjing 210093, China